11-2017

A Bidirectional Subsurface Remote Sensing Reflectance Model Explicitly Accounting for Particle Backscattering Shapes

Shuangyan He

Xiaodong Zhang
University of North Dakota, xiaodong.zhang2@UND.edu

Yuanheng Xiong

Deric Grey

[How does access to this work benefit you? Let us know!](#)

Follow this and additional works at: https://commons.und.edu/essp-fac

RESEARCH ARTICLE

Key Points:
- The bidirectional r_{rs} was analyzed and parameterized based on a theoretical derivation by Zaneveld (1982, 1995)
- The parameterized model explicitly accounts for particle backscattering shapes

A Bidirectional Subsurface Remote Sensing Reflectance Model Explicitly Accounting for Particle Backscattering Shapes

Shuangyan He[1,2], Xiaodong Zhang[1] [ID], Yuanheng Xiong[1], and Deric Gray[3]

[1]Department of Earth System Science and Policy, University of North Dakota, Grand Forks, ND, USA, [2]Ocean College, Zhejiang University, Hangzhou, China, [3]U.S. Naval Research Laboratory, Washington, DC, USA

Abstract The subsurface remote sensing reflectance (r_{rs}, sr^{-1}), particularly its bidirectional reflectance distribution function (BRDF), depends fundamentally on the angular shape of the volume scattering functions (VSFs, m^{-1} sr^{-1}). Recent technological advancement has greatly expanded the collection, and the knowledge of natural variability, of the VSFs of oceanic particles. This allows us to test the Zaneveld's theoretical r_{rs} model that explicitly accounts for particle VSF shapes. We parameterized the r_{rs} model based on HydroLight simulations using 114 VSFs measured in three coastal waters around the United States and in oceanic waters of North Atlantic Ocean. With the absorption coefficient (a), backscattering coefficient (b_b), and VSF shape as inputs, the parameterized model is able to predict r_{rs} with a root mean square relative error of ~4% for solar zenith angles from 0 to 75°, viewing zenith angles from 0 to 60°, and viewing azimuth angles from 0 to 180°. A test with the field data indicates the performance of our model, when using only a and b_b as inputs and selecting the VSF shape using b_b, is comparable to or slightly better than the currently used models by Morel et al. and Lee et al. Explicitly expressing VSF shapes in r_{rs} modeling has great potential to further constrain the uncertainty in the ocean color studies as our knowledge on the VSFs of natural particles continues to improve. Our study represents a first effort in this direction.

1. Introduction

A fundamental quantity describing the color of the ocean is the subsurface remote sensing reflectance (r_{rs}, sr^{-1}), formed as a ratio of the upwelling radiance, $L_u(\theta_s, \theta, \phi)$ to the downwelling irradiance, $E_d(\theta_s)$, with both defined just below the surface:

$$r_{rs}(\theta_s, \theta, \phi) \equiv \frac{L_u(\theta_s, \theta, \phi)}{E_d(\theta_s)}. \tag{1}$$

Here, θ_s represents the in-water solar zenith angle, θ the in-water sensor zenith angle, and ϕ the sensor azimuth angle relative to the solar plane. The r_{rs} is related to the inherent optical properties (IOPs) of absorption and backscattering coefficients (a and b_b) of the water body (Gordon, 1973; Morel & Prieur, 1977):

$$r_{rs}(\theta_s, \theta, \phi) = \frac{f'}{Q} \frac{b_b}{a + b_b}. \tag{2}$$

In equation (2), the f'/Q is called the bidirectional reflectance distribution function (BRDF), describing the angular variation of r_{rs} with the sun-viewing geometry. Many studies, some of which are cited in the following, used remote sensing reflectance (R_{rs}), defined just above the surface to describe the color of the ocean. Since the interface factor $\Re$, where $R_{rs} = \Re \times r_{rs}$, can be more or less considered as a constant for all practical purposes (Gordon, 2005), we will use r_{rs}, for simplicity, to represent either case of the definitions.

Both numerical simulations and field measurements showed that the BRDF factor varies with both sun-viewing geometries and the IOPs (Gleason et al., 2012; Gordon, 1989; Lee et al., 2011; Loisel & Morel, 2001; Morel et al., 1995, 2002; Morel & Gentili, 1991, 1993, 1996; Zhai et al., 2015), and it can vary up to 50% with IOPs and up to 100% with sun-viewing geometries as shown in Loisel and Morel (2001) and Morel et al. (2002). It is clear from equation (2) that the BRDF factor needs to be known to estimate a and b_b from r_{rs}, or to predict r_{rs} from a and b_b. Also, correction of the BRDF effect is important for vicarious calibration of an ocean color sensor because the radiance measured in the field and observed in a satellite pixel are often associated with different viewing geometries.

Since the BRDF factor has been scarcely measured in the field, its prediction relies essentially on numerical simulations (Hirata et al., 2009; Hlaing et al., 2012; Lee et al., 2011; Loisel & Morel, 2001; Morel et al., 2002; Morel & Gentili, 1991, 1993, 1996; Park & Ruddick, 2005). Using Monte Carlo simulation, Morel and Gentili (1991, 1993, 1996) parameterized f'/Q as a function of chlorophyll concentration in case 1 waters. Further improvements were made by accounting for Raman scattering and changes of particle phase function (PF) with chlorophyll concentration (Morel et al., 2002), resulting in a look-up-table (LUT) of f'/Q with 13 azimuth angles, 17 viewing zenith angles, 6 solar zenith angles, 6 chlorophyll concentrations, and 7 wavelengths. The particle PFs used in the simulation were generated as a linear combination of two PFs, one with backscattering ratio of 1.4% and the other of 0.19%, intended to represent small and large particles, respectively. Currently, this precompiled LUT is widely used for the BRDF correction. However, this method requires the knowledge of chlorophyll concentrations and was designed for Case 1 waters with a maximum chlorophyll concentration of 10 mg m^{-3} (Morel et al., 2002).

Park and Ruddick (2005) and Hlaing et al. (2012) developed a fourth-order and a third-order polynomial fittings of $r_{rs} = \sum_{i=1}^{4} g_i \left(\frac{b_b}{a+b_b} \right)^i$ and $r_{rs} = \sum_{i=1}^{3} g_i \left(\frac{b_b}{a+b_b} \right)^i$, respectively. In both cases, the Fournier–Forand (FF) (Fournier & Forand, 1994) PF was used and the coefficients g_i were tabulated as a function of sun-viewing geometry. Similarly, Lee et al. (2011) used a second-order polynomial to approximate the BRDF effect:

$$r_{rs} = \left(G_0^w + G_1^w \frac{b_{bw}}{a+b_b} \right) \frac{b_{bw}}{a+b_b} + \left(G_0^p + G_1^p \frac{b_{bp}}{a+b_b} \right) \frac{b_{bp}}{a+b_b}. \qquad (3)$$

A fundamental difference between the Lee et al. (2011) model and the models by Park and Ruddick (2005) and Hlaing et al. (2012) is that Lee et al. (2011) separately accounted for the molecular and particle backscattering (Lee et al., 2004). Also, in Lee et al. (2011), r_{rs} were simulated using a linear mixing of the Petzold average particle PF (Mobley, 1994) representing mineral particles and the FF PF (Fournier & Forand, 1994) with a backscattering ratio of 1% (1% FF) (Mobley et al., 2002) representing phytoplankton particles. A LUT was computed for G_0^w, G_1^w, G_0^p, and G_1^p as a function of 13 azimuth difference angles, 7 viewing zenith angles, and 6 solar zenith angles.

Zaneveld (1982, 1995) derived from the radiative transfer equation (RTE) a theoretical expression for r_{rs}. This analytical derivation provides a physical basis for evaluating the BRDF effect, which includes four components: the average cosine ($\bar{\mu}_d$) of downwelling radiance field, two shape factors describing backscattered downwelling radiance field (f_b) and forward scattered upwelling radiance field (f_L), and the diffuse attenuation coefficient of upwelling radiance (K_{Lu}). The Zaneveld derivation is not a true solution but a restatement of the RTE with the radiance distribution represented by f_b, f_L, and K_{Lu} (Zaneveld, 1995). Nevertheless, as pointed out by Zaneveld (1995), f_b and f_L vary in a relatively narrow range owing to the unique geometry of the light field and the particle scattering properties in the ocean, therefore it is possible to make approximations by relating them to the IOPs. The Zaneveld derivation has established an analytical basis, different from equation (2), for studying the BRDF effect.

Weidemann et al. (1995) investigated the error in retrieving particle backscattering (b_{bp}) from nadir-viewed r_{rs} due to uncertainties in the two shape factors, f_L and f_b. They found the error can vary from -20% to $+40\%$, primarily due to the uncertainty in f_b. They concluded that for r_{rs} inversion to be successful information about f_b must be included. Hoge et al. (2003) parameterized the Zaneveld (1995) shape factors using the Petzold average particle PF at 5 chlorophyll concentrations from 0.1 to 10.0 mg m^{-3}, 6 solar zenith angles from 0 to 60°, 1 viewing azimuth angle of 90°, and 10 wavelengths from 412 to 685 nm. Their model was able to predict the shape factors with a relative percentage error of 2–20%, and r_{rs} within 20%.

Studies have shown that the angular structure of bidirectional r_{rs} varies with the shape of the actual volume scattering functions (VSFs; β, m^{-1} sr^{-1}) in the ocean (Chami et al., 2006a; Gordon, 1989; Mobley et al., 2002; Morel et al., 2002; Morel & Gentili, 1991; Xiong et al., 2017; Zaneveld, 1982, 1995); however, the current r_{rs} models are built primarily using one particle phase function (Hoge et al., 2003; Morel & Gentili, 1991, 1993, 1996) or a linear combination of two (Hlaing et al., 2012; Lee et al., 2011; Morel et al., 2002; Park & Ruddick, 2005), because the VSFs had been scarcely measured (Morel et al., 2002). Recent technological advancement (Lee & Lewis, 2003; Sullivan & Twardowski, 2009) has greatly expanded the collection, and the knowledge of natural variability, of the VSFs of oceanic particles (Chami et al., 2005; Sullivan & Twardowski, 2009; Zhang et al., 2002,

2012). These measurements showed that the natural variability of VSFs is much greater than what had been known or assumed previously (Xiong et al., 2017). In this study, we will utilize the new VSF dataset to parameterize r_{rs} in an attempt to better understand the effect of VSF shapes on the BRDF. In particular, we will use the theoretical derivation of Zaneveld (1995) as an analytical basis to explicitly account for the shape of the VSFs.

2. Theoretical Basis

Zaneveld (1982, 1995) derived from the RTE the subsurface bidirectional r_{rs} for an optically deep ocean,

$$r_{rs}(\theta_s, \theta, \phi) = \frac{1}{2\pi\bar{\mu}_d(\theta_s)} \frac{f_b(\theta_s, \theta, \phi)}{g(\theta_s, \theta, \phi)} \frac{b_b}{a+b_b},$$

(4)

with

$$g(\theta_s, \theta, \phi) = 1 - \frac{K_{L_u}(\theta_s, \theta, \phi)}{a+b_b}\cos\theta - (f_L(\theta_s, \theta, \phi) - 1)\frac{b_f}{a+b_b},$$

(5)

by introducing two shape factors f_b and f_L, which were, respectively, defined as

$$f_b(\theta_s, \theta, \phi) \equiv \frac{\int_0^{2\pi}\int_0^{\pi/2} \beta(\gamma)L(\theta_s, \theta', \phi')\sin\theta'd\theta'd\phi'}{\frac{b_b}{2\pi}E_{od}(\theta_s)}$$

(6)

and

$$f_L(\theta_s, \theta, \phi) \equiv \frac{\int_0^{2\pi}\int_{\pi/2}^{\pi} \beta(\gamma)L(\theta_s, \theta', \phi')\sin\theta'd\theta'd\phi'}{L_u(\theta_s, \theta, \phi)b_f}.$$

(7)

In equations (4)–(7), K_{Lu} is the diffuse attenuation coefficient for upwelling radiance, $\bar{\mu}_d$ the downwelling average cosine, E_{od} the scalar downwelling irradiance, L the radiance distribution, c the attenuation coefficient, b_f the forward scattering coefficient, and $\beta(\gamma)$ the VSF at the scattering angle γ formed between the incident light traveling in direction (θ, ϕ) and the scattered light traveling in direction (θ, ϕ), and $\cos\gamma = \cos\theta\cos\theta' - \sin\theta\sin\theta'\cos(\phi-\phi')$.

Assuming β continuous in $(\pi/2, \pi)$ and using the second mean value theorem for definite integrals, f_b in equation (6) can be rewritten as

$$f_b(\theta_s, \theta, \phi) = \frac{\beta(\gamma_m)\int_0^{2\pi}\int_0^{\pi/2} L(\theta_s, \theta', \phi')\sin\theta'd\theta'd\phi'}{\frac{b_b}{2\pi}E_{od}(\theta_s)} = \frac{2\pi\beta(\gamma_m)}{b_b},$$

(8)

where

$$\beta(\gamma_m) = \frac{\int_0^{2\pi}\int_0^{\pi/2} \beta(\gamma)L(\theta_s, \theta', \phi')\sin\theta'd\theta'd\phi'}{\int_0^{2\pi}\int_0^{\pi/2} L(\theta_s, \theta', \phi')\sin\theta'd\theta'd\phi'},$$

(9)

and γ_m represents the mean scattering angle between the downwelling radiance field and the upwelling radiance to be observed. The exact value of γ_m depends on both the shape of VSF and downwelling radiance distribution. As shown in equation (8), the value of $f_b(\theta_s,\theta,\phi)$ does not depend on the exact geometry of (θ_s,θ,ϕ) but is related to the mean scattering angle γ_m; therefore, for simplicity, we will use $f_b(\gamma_m)$ to represent $f_b(\theta_s,\theta,\phi)$ hereafter. Equation (6) that defines $f_b(\gamma_m)$ can be deduced through equation (8) to a ratio of $\beta(\gamma_m)$ to b_b. Ignoring γ_m for a moment, equation (8) shows that the functional form of f_b is the inverse of the χ factor ($\chi = b_b/2\pi\beta$) (Oishi, 1990; Zhang et al., 2014a). However, the exact value of γ_m depends on the light field and the sun-viewing geometry, and so is $f_b(\gamma_m)$. Despite this, equation (8) provides a theoretical basis of using the χ factor to simulate $f_b(\gamma_m)$.

By further separating $\beta(\gamma_m)$ in equation (8) into molecular, $\beta_w(\gamma_m)$ and particle, $\beta_p(\gamma_m)$ components, we have

$$f_b(\gamma_m) = \frac{b_{bw}}{b_b} f_{bw}(\gamma_m) + \frac{b_{bp}}{b_b} f_{bp}(\gamma_m), \qquad (10)$$

where

$$f_{bp}(\gamma_m) = \frac{2\pi\beta_p(\gamma_m)}{b_{bp}} \qquad (11)$$

and

$$f_{bw}(\gamma_m) = \frac{2\pi\beta_w(\gamma_m)}{b_{bw}}. \qquad (12)$$

Combining equations (4) and (10), we have the bidirectional r_{rs} model that we will use for its parameterization in this study:

$$r_{rs}(\theta_s, \theta, \phi) = \frac{1}{2\pi\bar{\mu}_d(\theta_s)g(\theta_s, \theta, \phi)} \left(f_{bw}(\gamma_m)\frac{b_{bw}}{a+b_b} + f_{bp}(\gamma_m)\frac{b_{bp}}{a+b_b} \right). \qquad (13)$$

In equation (13), the shape of the VSF, while also affects g, is explicitly represented in the two shape factors, f_{bw} and f_{bp}.

3. Data and Methods

The VSFs were measured in coastal waters of the US (Chesapeake Bay, Mobile Bay, and Monterey Bay) with chlorophyll concentrations ranging from 1.4 to 40 mg m^{-3} and in open waters of North Atlantic Ocean with chlorophyll concentrations from 0.07 to 1.40 mg m^{-3} using a prototype Multispectral Volume Scattering Meter (MVSM) at eight wavelengths and a commercial LISST-100X at 532 nm (Type B; Sequoia Scientific, Inc.). The VSFs by LISST-100X at angles from 0.07 to 9.4° and the VSFs by MVSM at 532 nm from 9.5 to 179° were combined to form a near complete angular resolution of the scattering (Zhang et al., 2012). Altogether, there are 114 measured VSFs. The use of these VSFs and their validations have been reported in several studies (Zhang et al., 2012, 2013, 2014a, 2014b , 2017; Zhang & Gray, 2015). Removing the scattering due to pure seawater (Zhang et al., 2009) from these measured VSFs, we estimated the phase functions due to particles (Figure 1), which exhibit a backscattering ratio varying 0.15–5.4%. For comparison, the backscattering ratios for the particle PFs vary from 0.19 to 1.4% in Morel et al. (2002) and from 1.0 to 1.8% in Lee et al. (2011). The PFs shown in Figure 1 were used in this study to represent the varying angular scattering by oceanic particles.
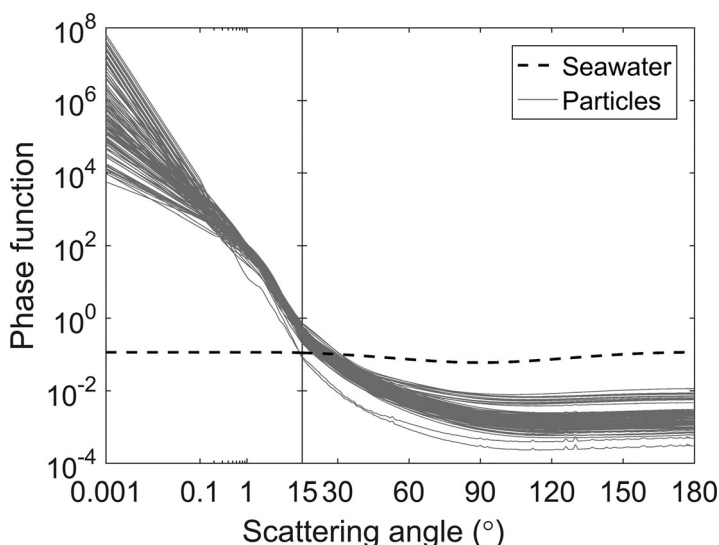
HydroLight (Mobley, 1995) was used to simulate the light field. The IOPs, required as inputs for HydroLight, were generated following the IOCCG Report 5 (IOCCG, 2006). A total of 100 sets of spectral a and b_b at 532 nm ($b_b/(a + b_b) \approx 0.03 – 0.30$; $b_{bp}/(a + b_b) \approx 0.01 – 0.30$) were generated using 20 chlorophyll concentrations (Chl = 0.03–30.0 mg m^{-3}) and five phytoplankton specific absorption spectrum. For each set of a and b_b, 114 PFs were used to represent different particle assemblages, generating a total of 114,000 (=100 × 114) sets of IOPs (a, b, b_b, and PF). The viewing zenith angles in air were set from 0 to 60° at an interval of 10°, the solar zenith angles in air from 0 to 75° at an interval of 15°, and the viewing azimuth angles relative to the sun from 0 to 180° at an interval of 45°. The simulation generated a total of 1,778,400 (=5 × 5 × 6 × 100 × 114 + 1 × 1 × 6 × 100 × 114) sets of AOPs at 532 nm. The simulated downwelling irradiance, upwelling and downwelling radiance distribution at depths of 0$^-$ (just below the surface) and 0.01 m were used to estimate the parameters of f_b, g, and $\bar{\mu}_d$ in equation (13).

Figure 1. Phase functions at 532 nm computed for pure seawater and estimated for particles from the measured VSFs. The x-axis is in logarithmic scale at angles <15° and in linear scale at larger angles.

f_L was estimated following equation (7) using the input β and HydroLight-simulated upwelling radiance distribution at the depth of 0^-. $\beta(\gamma_m)$ was estimated following equation (9), and the value of γ_m was found by matching the estimated $\beta(\gamma_m)$ with the input β. With γ_m, $f_{bp}(\gamma_m)$, and $f_{bw}(\gamma_m)$ were estimated following equations (11) and (12), respectively.

4. Results

4.1. Comparison of the HydroLight Simulation and the Zaneveld (1995) Model Prediction

Even though both HydroLight and the Zaneveld model are based on the same RTE, it is expected that the detailed numerical implementations would introduce uncertainty. To establish a baseline of uncertainty that is due to numerical implementation, we compare r_{rs} calculated from equation (13) with the HydroLight simulation (Figure 2).

The two methods agreed with each other within 2.4% (standard deviation (SD) = 0.024 sr^{-1}, Figure 2b). The Zaneveld model-predicted r_{rs} seemed to be slightly less than the HydroLight-simulated values for $r_{rs} > 0.02$ (Figure 2a). Relatively greater differences were also found for both off-nadir viewing geometries and for more peaked phase functions. This is mainly due to the uncertainty introduced in the numerical integration for calculating f_L, which depends strongly on the shape of phase functions at near forward angles, particularly for off-nadir viewing geometries. Nevertheless, the relative difference in r_{rs} of 2.4% between the Zaneveld model and the HydroLight simulation is less than half of the 6% uncertainty reported in Mobley et al. (1993), which compared six numerical models in simulating water-leaving radiance.

To eliminate this inherent uncertainty due to performing numerical integration, which is also extremely time consuming, the g factor, which contains f_L (equation (5)), was estimated reversely using calculated f_b, $\bar{\mu}_d$, and r_{rs}, and inputs of a and b_b following equation (4). The similar approach was used in Weidemann et al. (1995).

4.2. Parameterization of r_{rs}

4.2.1. Shape Factor f_b

Equation (10) shows that the shape factor $f_b(\gamma_m)$ can be partitioned into backscattering weighted contributions due to pure seawater ($f_{bw}(\gamma_m)$) and particles ($f_{bp}(\gamma_m)$). The exact value of $f_b(\gamma_m)$ also depends on the mean scattering angle γ_m. The values of γ_m, as shown in Figure 3, are generally greater than $\pi/2$, indicating the importance of the backscattering process in regulating f_b. Because the downwelling radiance field nearly always shows a dominant or maximum radiance at the angle of refracted solar disk just beneath the sea surface, a single-scattering approximation has been used to estimate $f_b(\gamma_m)$ as $f_b(\gamma_m) = \frac{2\pi\beta(\gamma_m)}{b_b} \approx \frac{2\pi\beta(\gamma_s)}{b_b}$ (Hoge et al., 2003; Weidemann et al., 1995; Zaneveld, 1995), where γ_s represents the scattering angle formed between the subsurface sun and the viewing vector. While γ_m is closely related to γ_s, which is fixed for a given sun-viewing geometry, they are different in values (Figure 3) as a result of multiple scattering. Therefore, we would also expect $f_b(\gamma_m) \neq f_b(\gamma_s)$. As an example, variations of $f_{bp\gamma}(\gamma_m)$ and $f_{bw\gamma}(\gamma_m)$ with γ_s are shown in Figure 4 for two particle PFs ($b_{bp}/b_p = 0.0045, 0.0312$). Clearly, $f_{bp}(\gamma_m)$ and $f_{bw}(\gamma_m)$ (colored dots in Figure 4) covary with, but differ from, their respective single scattering counterparts, $f_{bp}(\gamma_s)$ and $f_{bw}(\gamma_s)$ (red lines in Figure 4). Over the entire data set, the best fits of $f_{bp}(\gamma_m)$ and $f_{bw}(\gamma_m)$ (black lines in Figure 4) are:
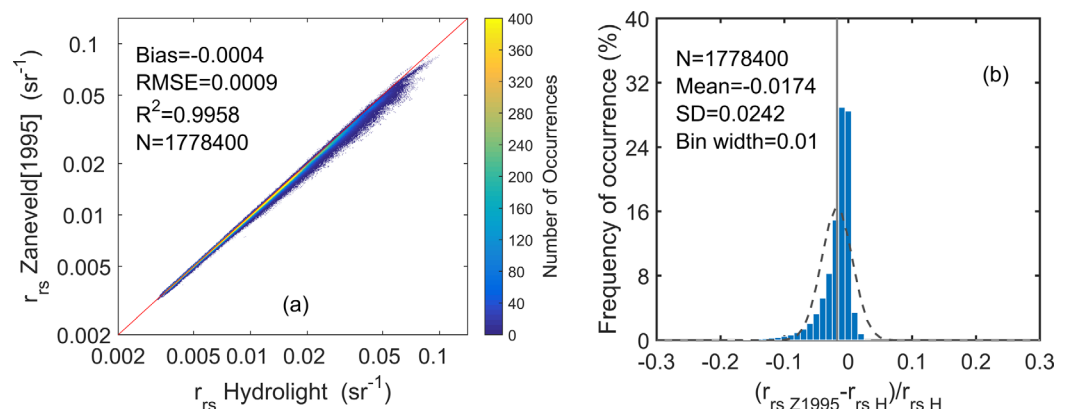

Figure 2. Comparison of r_{rs} between the Zaneveld (1995) model and the HydroLight simulation.
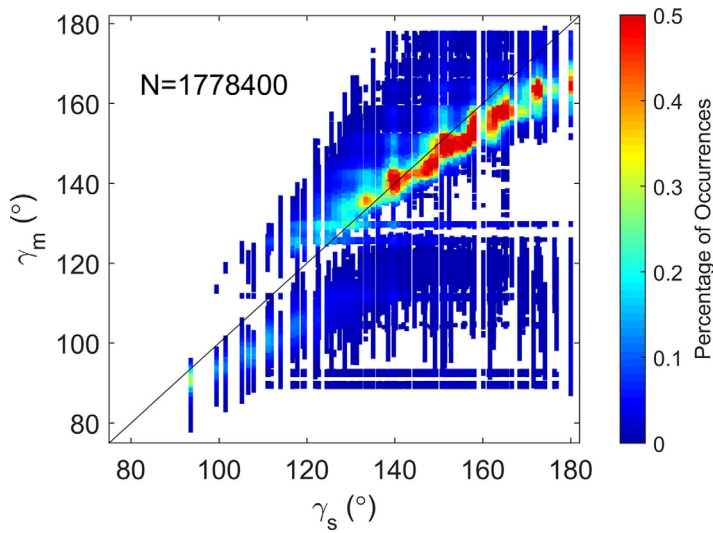
Figure 3. The comparison of single scattering angles (γ_s) estimated for the sun-viewing geometries used in the simulation and the corresponding mean scattering angles (γ_m) estimated using equation (9).

$$f_{bw}(\gamma_m) = f_{bw}(\gamma_s) - 0.2811(f_{bw}(\gamma_s) - 0.9407) + 0.0318, \quad (14)$$

$$f_{bp}(\gamma_m) = f_{bp}(\gamma_s) - 0.3919(f_{bp}(\gamma_s) - 0.9314) + 0.0369, \quad \gamma_s \geq 120°;$$
$$= f_{bp}(\gamma_s) + 0.1540(f_{bp}(\gamma_s) - 0.9314) + 0.0369, \quad \gamma_s < 120°.$$
$$(15)$$

In equation (14), $f_{bw}(\gamma_s)$ was calculated following equation (12) as the inverse of the χ factor for pure seawater at angle γ_s, and therefore can be considered as known (Zhang et al., 2009) for a given sun-viewing geometry. Similarly, $f_{bp}(\gamma_s)$ in equation (15) was calculated following equation (11) as the inverse of the χ factor for particles at angle γ_s, which, however, is expected to vary with the size, shape and composition of the particles (Zhang et al., 2014a). Therefore, $f_{bp}(\gamma_s)$ is generally unknown and needs to be provided.

4.2.2. Factor g

Factor g represents a combined effect due to the shape factor f_L, K_{Lu}, and the IOPs of a, b_b, and b_f (equation (5)). Figure 5 shows the variation of $1/g$ as a function of $b_{bp}/(a + b_b)$ for different particle PFs (indicated by $\beta_p(30°)/\beta_p(120°)$ values) and for two viewing geometries. Since f_L and b_f are mainly due to forward scattering, which in oceanic waters is expected to be dominated by the particle scattering, the g values increase with the forward steepness of particle PFs, measured as $\beta_p(30°)/\beta_p(120°)$. We used $\beta_p(30°)/\beta_p(120°)$ to represent the forward shape of particle PFs because both theoretical simulations and field measurements show that β_p exhibits minimal variability at 120° (Boss & Pegau, 2001; Dall'Olmo et al., 2009; Maffione & Dana, 1997; Oishi, 1990; Sullivan & Twardowski, 2009; Zhang et al., 2014a), and the PF shapes at angles <15° have a negligible influence on r_{rs} (Gordon, 1993). The g factor was parameterized as:

$$g = m_0 + m_1\left(\frac{b_{bw}}{a+b_b}\right) + m_2\left(\frac{b_{bp}}{a+b_b}\right) + m_3\left(\frac{b_{bp}}{a+b_b}\right)^2. \quad (16)$$

A LUT was built for coefficients m_{0-3} as functions of sun-viewing geometries and values of $\beta_p(30°)/\beta_p(120°)$. A sample of the LUT is listed in Table 1.
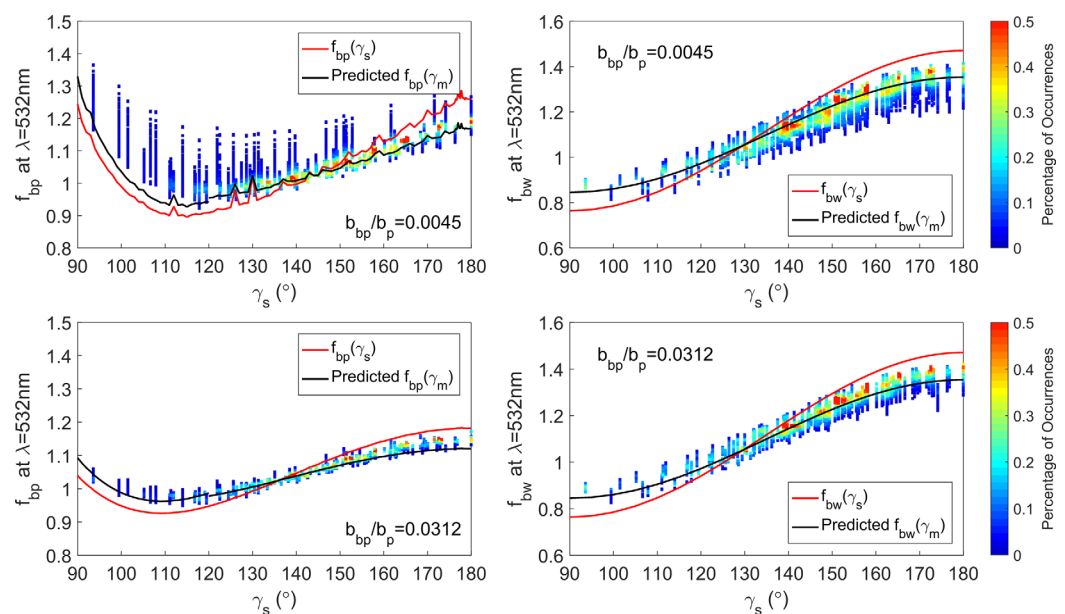

Figure 4. Variations of $f_{bp}(\gamma_m)$ and $f_{bw}(\gamma_m)$ at 532 nm with γ_s simulated for two particle PFs with different b_{bp}/b_p values. Red lines are $f_{bp}(\gamma_s)$ and $f_{bw}(\gamma_s)$ and black lines are predicted $f_{bp}(\gamma_m)$ and $f_{bw}(\gamma_m)$ using equations (14) and (15), respectively.
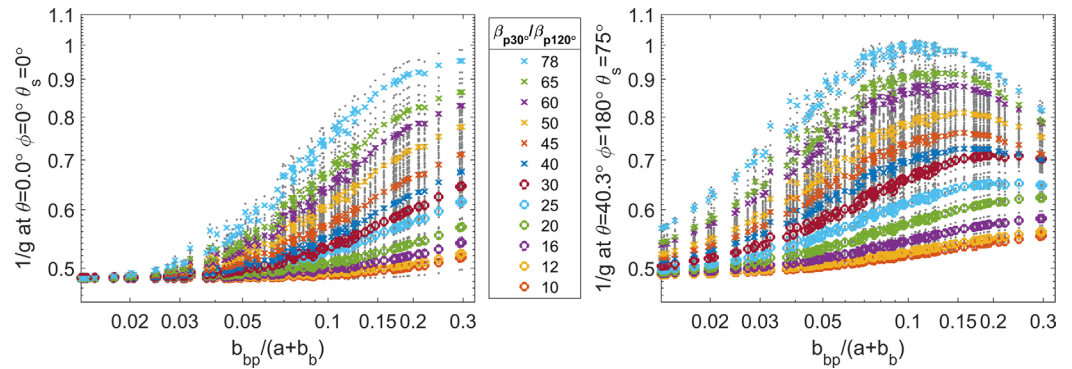
Figure 5. Variation of $1/g$ at 532 nm with $b_{bp}/(a+b_b)$ and $\beta_p(30°)/\beta_p(120°)$ at two sun-viewing geometries. The gray dots are the estimated $1/g$ values from HydroLight and the colored symbols are the estimation from equation (16) for the 12 $\beta_p(30°)/\beta_p(120°)$ values shown in the legend.

4.2.3. Downwelling Average Cosine $\bar{\mu}_d$

The average cosine has been used as a simple, but for most purposes, sufficient parameter describing the directional structures of the light field (Kirk, 1981; Mobley, 1994). It has been empirically related to the diffuse attenuation coefficient of downwelling irradiance, K_{Ed}, and the absorption coefficient (Kirk, 1981; Nahorniak et al., 2001). Figure 6 shows that $\bar{\mu}_d$ generally increases with cosine of the solar zenith angles. In this study, $\bar{\mu}_d$ was parameterized as:

$$\bar{\mu}_d = f_1\left(1+f_2\cos\theta_s+f_3\cos^2\theta_s\right)\left(1+f_4\frac{a}{K_{E_d}}\right), \tag{17}$$

where f_1, f_2, f_3, and f_4 are 0.4779, -0.0641, 0.2660, and 0.7164. We used the Lee et al. (2005) model for K_{Ed}:

$$K_{Ed} = (1+k_1\theta_s)a + k_2\left(1+k_3 e^{(-k_4a)}\right)b_b, \tag{18}$$

where k_1, k_2, k_3, and k_4 are 0.3771, 0.4986, 2.5345, and 0.0852.

4.3. Performance of Parameterizations for r_{rs}

For a given sun-viewing geometry and assuming the IOPs for pure seawater are known, the parameterized r_{rs} model requires the inputs of a and b_b as well as a measure of particle PF. Specifically, f_{bp} and b_{bp} are needed to simulate f_b; a, b_{bp}, and ratio of $\beta_p(30°)/\beta_p(120°)$ for g; and a and b_{bp} for $\bar{\mu}_d$. Figure 7 evaluates the performance of combined and individual parameterizations of f_b, g, and $\bar{\mu}_d$ for predicting the bidirectional r_{rs}. Overall, the parameterized model was able to predict r_{rs} with virtually no bias and an absolute uncertainty (as measured by root mean square error) of 0.0010 sr^{-1} (Figure 7a) or a relative uncertainty of 3.5% (as measured by root mean square relative error) (Figure 7b). The uncertainties due to parameterizing f_b and g were comparable, of about 0.0007 sr^{-1} (Figure 7c) or 2.2% (Figure 7d) and 0.0007 sr^{-1} (Figure 7e) or

Table 1
The Values of the Coefficients m_{0-3} at Five Sun-Viewing Geometries and Two Ratios of $\beta_p(30°)/\beta_p(120°)$

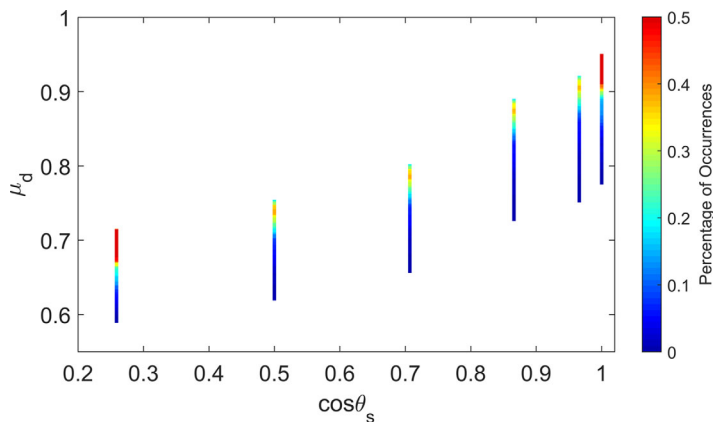| $\beta_{p30°}/\beta_{p120°}$	θ_s in air	θ in air	ϕ	m_0	m_1	m_2	m_3
12	0°	0°	0°	2.0532	−0.1999	0.6349	−1.0137
	30°	40°	90°	1.9708	−0.6163	0.3815	−0.0593
	30°	40°	135°	1.9742	−1.0619	0.4090	0.8819
	60°	40°	90°	2.1515	−1.1224	0.3680	1.0685
	60°	40°	135°	2.1444	−1.6832	0.3510	2.2380
60	0°	0°	0°	2.1110	−6.8176	4.5799	12.8944
	30°	40°	90°	1.8932	−7.3510	6.1285	17.0894
	30°	40°	135°	1.8303	−8.0507	6.9631	19.7766
	60°	40°	90°	2.0265	−7.9635	6.4476	19.6354
	60°	40°	135°	1.8892	−8.6473	7.7785	22.8834

Figure 6. Variation of $\bar{\mu}_d$ with solar zenith angles.

2.7% (Figure 7f), respectively. The smallest source of uncertainty was in modeling $\bar{\mu}_d$, which had an uncertainty of about 0.0003 sr^{-1} (Figure 7g) or 1.6% (Figure 7h).

5. Discussion and Conclusions

On the basis of a theoretical derivation by Zaneveld (1982, 1995), the bidirectional r_{rs} was analyzed through equation (4), in which the BRDF is separated into three components of f_b, g, and $\bar{\mu}_d$. These three components were parameterized using HydroLight simulations using 114 particle PFs measured in both coastal and oceanic waters. The comparison with simulated data shows that the developed model, with inputs of a, b_b, and the particle PF, is able to predict r_{rs} at 532 nm with an absolute uncertainty of <0.001 sr^{-1} (Figure 7a) and a relative uncertainty <4% (Figure 7b).

As explained in Zaneveld (1995) and derivable from equation (4), if the VSF is isotropic in the backward angles ($=\frac{b_b}{2\pi}$) and isotropic in the forward angles ($=\frac{b_f}{2\pi}$) and the upwelling radiance field is also isotropic ($=L_u(\theta_s, \theta, \phi)$), $r_{rs} = \frac{1}{2\pi\bar{\mu}_d(1-D\cos\theta)}\frac{b_b}{a+b_b}$, where $D = \frac{K_{Lu}}{a+b_b}$. Under single scattering assumption, $\bar{\mu}_d = \cos\theta_s$ and $D\cos\theta_s \approx 1$ (varying between 0.8 and 1.2), the above r_{rs} equation approximates the quasi-single-scattering derivation for r_{rs}, i.e., $r_{rs} \approx \frac{1}{2\pi(\cos\theta_s - \cos\theta)}\frac{b_b}{a+b_b}$ (Gordon, 1973). The multiple scattering, the asymmetric upwelling light field, and the anisotropic scattering by oceanic particles in either forward or backward angles, would cause the deviation of r_{rs} from this isotropic, single scattering value by a factor $= \frac{(\cos\theta_s - \cos\theta)}{\bar{\mu}_d}\frac{f_b(\gamma_m)}{g}$. The $f_b(\gamma_m)$ represents the correction due to the anisotropic VSF shape in the backward angles. The values of $f_b(\gamma_m)$ vary approximately between 0.9 and 1.5 (Figure 4), depending on the mean scattering angle (γ_m) and the nature of particle assemblage (Zhang et al., 2017). Since the values of f_b are mostly >1, the effect of deviation of the actual shape of the VSF in the backward angles from the isotropic form of $\frac{b_b}{2\pi}$ is to increase r_{rs}. Factor g represents the correction due to the anisotropic VSF shape in the forward angles and the anisotropic upwelling radiance field. The values of $1/g$ vary approximately between 0.5 and 1.0 over the entire dataset (Figure 5) and between 0.5 and 0.75 for $b_{bp}/(a+b_b) < 0.05$, which represents typical oceanic waters. Overall, the values of $1/g$ are <1, indicating the combined effect of anisotropic upwelling radiance field as well as the deviation of forward VSF shape from the isotropic form of $\frac{b_f}{2\pi}$ is to lower r_{rs}.

Since models by Morel et al. (2002) and Lee et al. (2011) have been frequently used in describing the bidirectional remote sensing reflectance, we compare our model with these two in Table 2. Following equation (4), the BRDF factor in the Morel et al. (2002) model is effectively $\frac{1}{2\pi\bar{\mu}_d}\frac{f_b(\gamma_m)}{g}$. The effect of VSF shape was implicitly contained in chlorophyll concentration, which determines the mixing ratio of two PFs with b_{bp}/b_p ratios of 0.19 and 1.4%, respectively. Equation (10) shows that f_b is inherently contributed by two components, f_{bw} due to seawater and f_{bp} due to particles. Therefore, to more explicitly express the BRDF effect, a logical step is to separate the contributions by seawater and particles. This improvement was achieved by Lee et al. (2011). In their model (equation (3)), the BRDF factors due to seawater and particles are $G_0^w + G_1^w\frac{b_{bw}}{a+b_b}$ and $G_0^p + G_1^p\frac{b_{bp}}{a+b_b}$, which are effectively $\frac{1}{2\pi}\frac{f_{bw}(\gamma_m)}{\bar{\mu}_d g}$ and $\frac{1}{2\pi}\frac{f_{bp}(\gamma_m)}{\bar{\mu}_d g}$, respectively. Even though Lee et al. (2011) used varying VSF shapes in their simulations, their model parameters only have sun-viewing geometries as inputs; therefore their BRDF factor only includes a statistic average of the shape effect. Our approach more or less combined these two methods by (1) separating seawater and particles as in Lee et al. (2011) and (2) treating particle VSF shapes individually as in Morel et al. (2002). A further improvement in our approach is to explicitly express the VSF shape using the Zaneveld's theoretical formula. In addition, the VSF shapes used in our model are all based on field measurements, which exhibit a much greater variability in the VSF shape than the other two models have used (Xiong et al., 2017).

Despite its analytical derivation from the RTE, our model is more complex and requires inputs of the sun-viewing geometry, the IOPs of a and b_b, and the VSF shapes. The IOPs of pure seawater, including a_w and β_w are known quantities (Morel, 1974; Pope & Fry, 1997; Zhang et al., 2009), and particle IOPs of a_p and b_{bp} are retrievable from ocean color remote sensing (Lee et al., 2002; Werdell et al., 2013). This leaves out the particle VSF shapes. Zhang et al. (2017) recently showed that oceanic f_{bp}(90–180°) can be very well
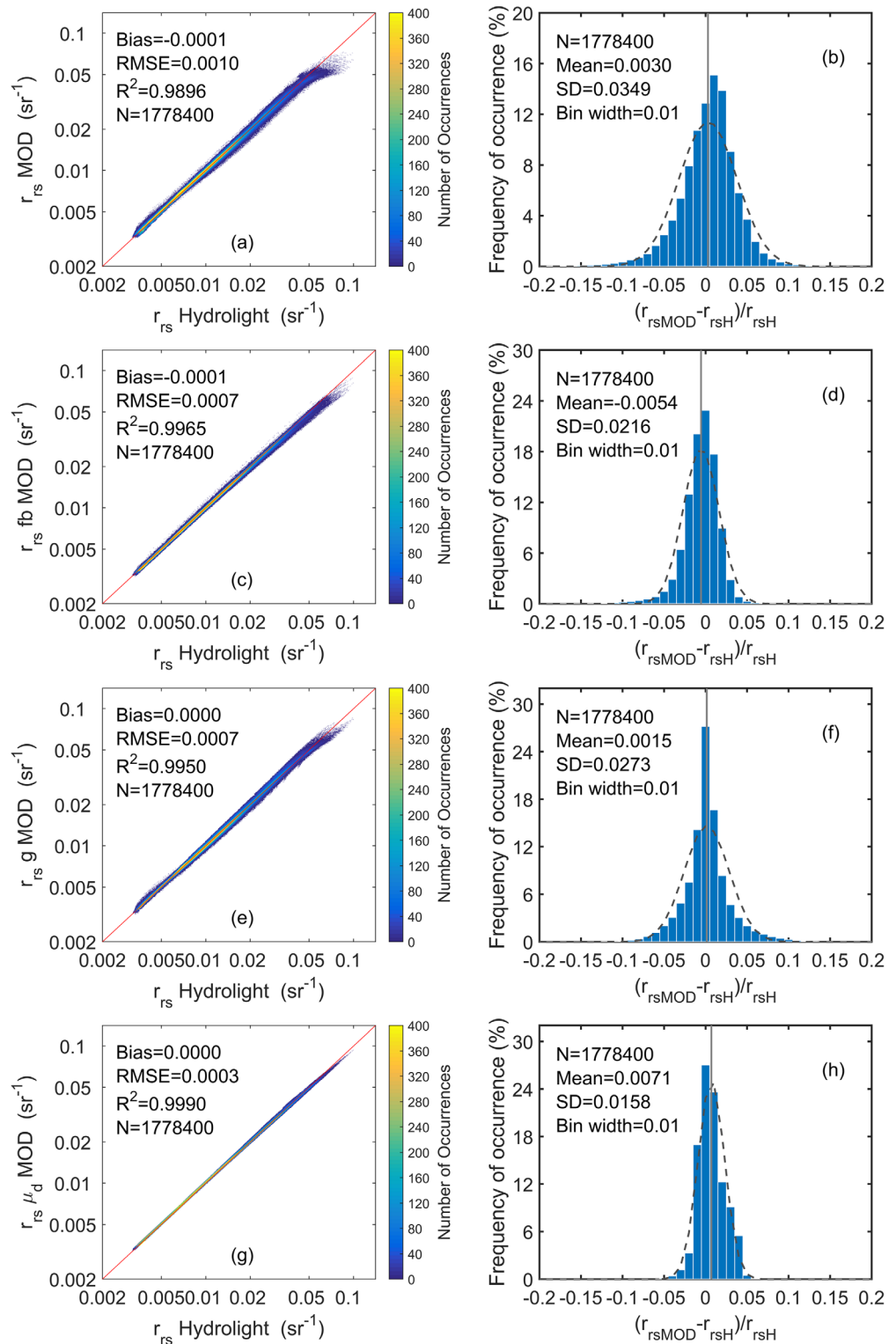
Figure 7. Comparison of r_{rs} between our parameterized Zaneveld model (r_{rsMOD}) and the HydroLight simulation (r_{rsH}). In (a) and (b), all the three factors in equation (4), i.e., f_b, g, and $\bar{\mu}_d$, were estimated using the parameterized models. In (c) and (d) only f_b was estimated using the parameterized model; (e) and (f) only g was estimated using the parameterized model; and (g) and (h) only $\bar{\mu}_d$ was estimated using the parameterized model.

Table 2
Summary of Three Bidirectional r_{rs} Models

	Morel et al. (2002)	Lee et al. (2011)	This study
Input	Chl, (θ_s, θ, ϕ)	$a, b_b, (\theta_s, \theta, \phi)$	$a, b_b, (\theta_s, \theta, \phi), f_{bp}, \beta_p(30°)/\beta_p(120°)$
Model details	$r_{rs} = \frac{f'}{Q}\frac{b_b}{a+b_b}$	$r_{rs} = \left(G_0^w + G_1^w \frac{b_{bw}}{a+b_b}\right)\frac{b_{bw}}{a+b_b} + \left(G_0^p + G_1^p \frac{b_{bp}}{a+b_b}\right)\frac{b_{bp}}{a+b_b}$	$r_{rs} = \frac{1}{2\pi\bar{\mu}_d}\frac{f_{bw}}{g}\frac{b_{bw}}{a+b_b} + \frac{1}{2\pi\bar{\mu}_d}\frac{f_{bp}}{g}\frac{b_{bp}}{a+b_b}$
Main features	(1) LUT of f' and Q with λ, Chl and sun-viewing geometries; (2) operationally used in ocean color data processing	(1) Separating the effects due to seawater and particles; (2) LUT of spectrally independent G_i^w and G_i^p with sun-viewing geometries	(1) Separating the effects due to seawater and particles; (2) explicitly expressed as a function of backward VSF shapes of seawater, f_{bw} and of particles f_{bp}
How are the VSFs treated in the model	(1) The particle VSFs are represented by a combination of two PFs with b_{bp}/b_p of 0.19 and 1.4%; (2) the effect of VSF shapes is implicitly contained as a function of Chl	(1) The particle VSFs are represented by a combination of two PFs, with b_{bp}/b_p of 1.0 and 1.8%; (2) the effect of VSF shapes is statistically averaged	(1) The particle VSFs are based on 114 measurements with b_{bp}/b_p ranging 0.15–5.4%; (2) requires the VSF shapes as additional input

represented by a linear mixing of two end members, one representing the f_{bp} for particles of sizes much smaller than the wavelength and the other for particles of sizes much greater than the wavelength. Zhang et al. (2017) also showed that the mixing ratio can be predicted by b_{bp}. In addition, from the measured VSF data used in this study, we found that $\beta_p(30°)/\beta_p(120°)$ can be related to $\beta_p(90°)/\beta_p(120°)$, which is the same as $f_{bp}(90°)/f_{bp}(120°)$:

$$\frac{\beta_p(30°)}{\beta_p(120°)} = 63.70\frac{f_{bp}(90°)}{f_{bp}(120°)} - 56.98. \tag{19}$$

Therefore, both f_b and $\beta_p(30°)/\beta_p(120°)$ can be predicted from b_{bp} using the Zhang et al. (2017) two-component model. Such an implementation (Figure 8) is tested in Figure 9. From the NASA's bio-Optical Marine Algorithm Dataset (NOMAD) (Werdell & Bailey, 2005) and SeaWiFS Bio-optical Archive and Storage System (SeaBASS) (Werdell & Bailey, 2002; Werdell et al., 2003), we found a total of 82 sets of data with concurrent measurements of chlorophyll concentration, a, b_b, and nadir-viewed r_{rs} collected in three different waters: 25 in the coastal water of Japan and North Pacific Ocean, 30 in Chesapeake Bay, and 27 in Lake Superior (Figure 9a). With only a and b_b as inputs, our model (Figure 8) was able to predict r_{rs} with a root mean square error of 0.0011 sr^{-1} and root mean square relative error of 15% (Figure 9b). For comparison, the absolute and relative errors are 0.0012 sr^{-1} and 15% for the Lee et al. (2011) model, and 0.0013 sr^{-1} and 19% for the Morel et al. (2002) model. Comparing to measured radiance distribution in various Case I and Case II waters, Gleason et al. (2012) found that both Morel et al. (2002) and Lee et al. (2011) models can simulate the BRDF effect, agreeing generally within ±20% of the measurements. Relatively, however, they found the Morel et al. (2002) model, which implicitly includes variable particle VSF shapes as a function of chlorophyll concentration (Table 2), performs better in case I waters, indicating the importance of the VSF shapes in modeling the bidirectional r_{rs}. On the other hand, the Lee et al. (2011) model, which only represents an average shape effect (Table 2), performs better in Case II water at small azimuth angles and for chlorophyll concentration >10 mg m^{-3}, for which Gleason et al. (2012) found the VSF shape effect is not important. Our results (Figure 9), which are mostly for coastal and inland waters, also show that these two models were generally comparable
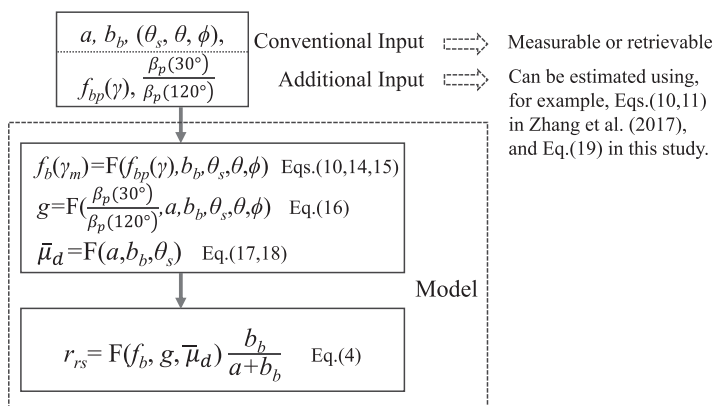

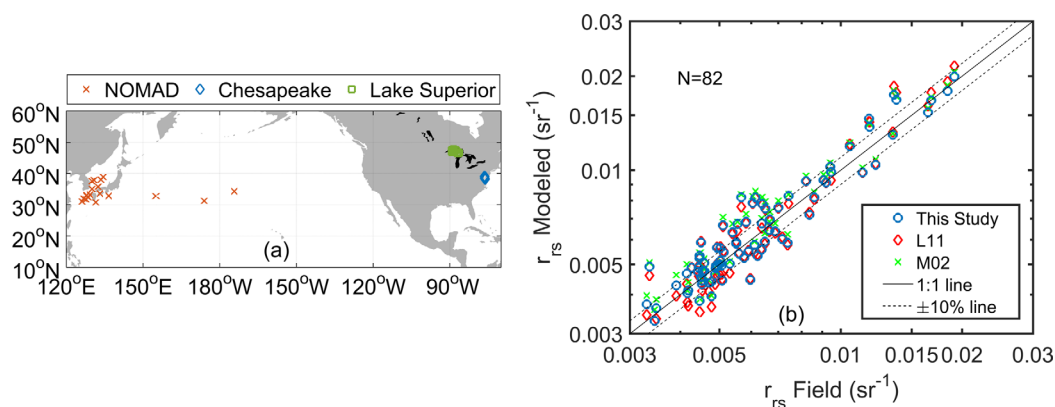**Figure 8.** Flowchart of an example to apply the r_{rs} model developed in this study.

Figure 9. (a) Field data with simultaneous measurements of a, b_b, and r_{rs}: 25 records from NOMAD in coastal and open North Pacific Ocean, 30 from SeaBASS in Chesapeake Bay, and 27 from SeaBASS in Lake Superior. (b) Measured r_{rs} are compared with predicted r_{rs} using our parameterized Zaneveld model, the Lee et al. (2011) model (L11), the Morel et al. (2002) model (M02).

(with Lee et al. slightly better than Morel et al.) in simulating the bidirectional r_{rs}. In addition, our model performed comparably same as (or marginally better than) these two models. However, since we could not find off-nadir viewed r_{rs} with simultaneously measured a and b_b, we only evaluated the BRDF effect due to the sun elevations.

Even though only the magnitude of the backward β (i.e., b_b) has been used in the current ocean color retrieval algorithms, the Zaneveld theoretical derivation shows that it is β—including both its magnitude and shape—that are actually measured in ocean color remote sensing. In fact, Jerlov (1976) pointed out that the variation of the diffuse reflectance with the sun elevation angle is a direct consequence of the shape of the VSF. Therefore, the shape of the backward β_p is contained in, and hence might be possibly estimated from, the measured r_{rs} (Gordon, 1989). Here, we demonstrated that a preliminary approach of estimating the backward shape of β_p and $\beta_p(30°)/\beta_p(120°)$ using b_{bp} following Zhang et al. (2017) and equation (19). Thus, only two unknowns (a and b_b) exist in the bidirectional r_{rs} model as sun-viewing geometries are usually known. The entire retrieval algorithm can be executed iteratively initiated by a first guess of a and b_b using the current ocean color retrieval algorithm (Figure 8).

We need to point out that the use of the Zhang et al. (2017) model and equation (19) to estimate the VSF shape is only one applicable example and can be improved. For example, we think the model developed in Zhang et al. (2017, equation (11)) for estimating the mixing ratio using b_{bp} is still preliminary. Nevertheless, we are encouraged by the results shown in Figure 9 that our model, despite its complexity, performed comparable to or slightly better than the currently used models by Morel et al. (2002) and Lee et al. (2011). As our knowledge of the VSFs of natural particles continues to improve, we expect that new and/or better algorithms will be developed to estimate the VSF shapes. This, in combination with our parameterized model based on Zaneveld's derivation, which explicitly accounts for the effect of VSF shapes on r_{rs}, offers great potential to further constrain the uncertainty in the ocean color studies. For example, a better BRDF correction is needed for the emerging geostationary ocean color remote sensing, which acquires images at a range of sun zenith angles versus the typical sun-synchronous polar orbiting ocean color sensors acquiring images at approximately fixed local sun zenith angle (Ruddick et al., 2014).

Our model is developed for 532 nm at which the VSFs were measured. Our current knowledge on the spectral variation of particle VSFs is limited (Chami et al., 2006b). Assuming the shape of VSFs is spectrally independent, we tested our model at other wavelengths. We found that only the g parameterization needs modification, whereas the f_b and $\bar{\mu}_d$ parameterizations work well at other wavelengths. The reason that g needs spectral adjustment is because g depends on the geometrical structure of incident light field, which varies spectrally. This dependence is carried through by f_L and K_{Lu} (equation (5)). Downwelling average cosine $\bar{\mu}_d$ also depends on the incident light field, but the dependence more or less cancels out as a ratio between E_{od} and E_d.

The effect of winds was not considered in our study. However, Morel and Gentili (1996) found that the impact of winds (0–10 m s^{-1}) on the angular r_{rs} is almost undetectable with solar zenith angles $<75°$ and

in-air viewing zenith angles $<42°$. A maximum variation of 10% can occur at chlorophyll concentration $= 3$ mg m^{-3} with the viewing zenith angle $> 42°$ and sun zenith angle $= 75°$. For typical sun-viewing geometries applicable to ocean color, they concluded that the BRDF factor can be safely corrected without considering varying wind speeds. Also, only elastic scattering is included in the HydroLight simulations, and inelastic Raman scattering was not considered in this study. Morel et al. (2002) found that the Raman contribution can be neglected in waters with chlorophyll concentration > 0.3 mg m^{-3}, but the contribution can be significant in more oligotrophic waters. For example, Gordon (1999) showed that at $\theta_s = 37°$ Raman scattering could contribute 10–20% of water-leaving radiance at 490–600 nm in a water with chlorophyll concentration <0.1 mg m^{-3}. However, since the angular distribution of Raman scattering is very similar in shape to the molecular scattering (Morel & Mueller, 2002), we expect that accounting for the Raman effect will probably only affect the seawater portion of our model and when particle content is low. A correction of Raman scattering to our r_{rs} model will be further investigated for oligotrophic waters.

References

Boss, E., & Pegau, W. S. (2001). Relationship of light scattering at an angle in the backward direction to the backscattering coefficient. *Applied Optics*, *40*(30), 5503–5507. https://doi.org/10.1364/AO.40.005503

Chami, M., McKee, D., Leymarie, E., & Khomenko, G. (2006a). Influence of the angular shape of the volume-scattering function and multiple scattering on remote sensing reflectance. *Applied Optics*, *45*(36), 9210–9220. https://doi.org/10.1364/AO.45.009210

Chami, M., Shybanov, E. B., Churilova, T. Y., Khomenko, G. A., Lee, M. E. G., Martynov, O. V., . . . Korotaev, G. K. (2005). Optical properties of the particles in the Crimea coastal waters (Black Sea). *Journal of Geophysical Research*, *110*, C11020. https://doi.org/10.1029/2005JC003008

Chami, M., Shybanov, E. B., Khomenko, G. A., Lee, M. E. G., Martynov, O. V., & Korotaev, G. K. (2006b). Spectral variation of the volume scattering function measured over the full range of scattering angles in a coastal environment. *Applied Optics*, *45*(15), 3605–3619. https://doi.org/10.1364/AO.45.003605

Dall'Olmo, G., Westberry, T. K., Behrenfeld, M. J., Boss, E., & Slade, W. H. (2009). Significant contribution of large particles to optical backscattering in the open ocean. *Biogeosciences*, *6*, 947–967. https://doi.org/10.5194/bg-6-947-2009

Fournier, G. R., & Forand, J. L. (1994). Analytic phase function for ocean water. In *Proceeding of SPIE* (Vol. 2258), *Ocean Optics XII*, Bergen, Norway. Bellingham WA: SPIE. http://dx.doi.org/10.1117/12.190063

Gleason, A. C. R., Voss, K. J., Gordon, H. R., Twardowski, M., Sullivan, J., Trees, C., . . . Lee, Z.-P. (2012). Detailed validation of the bidirectional effect in various Case I and Case II waters. *Optics Express*, *20*(7), 7630–7645. https://doi.org/10.1364/OE.20.007630

Gordon, H. R. (1973). Simple calculation of the diffuse reflectance of the ocean. *Applied Optics*, *12*(12), 2803–2804. https://doi.org/10.1364/AO.12.002803

Gordon, H. R. (1989). Dependence of the diffuse reflectance of natural waters on the sun angle. *Limnology and Oceanography*, *34*(8), 1484–1489. https://doi.org/10.4319/lo.1989.34.8.1484

Gordon, H. R. (1993). Sensitivity of radiative transfer to small-angle scattering in the ocean: Quantitative assessment. *Applied Optics*, *32*(36), 7505–7511. https://doi.org/10.1364/AO.32.007505

Gordon, H. R. (1999). Contribution of Raman scattering to water-leaving radiance: A reexamination. *Applied Optics*, *38*(15), 3166–3174. https://doi.org/10.1364/AO.38.003166

Gordon, H. R. (2005). Normalized water-leaving radiance: Revisiting the influence of surface roughness. *Applied Optics*, *44*(2), 241–248. https://doi.org/10.1364/AO.44.000241

Hirata, T., Hardman-Mountford, N., Aiken, J., & Fishwick, J. (2009). Relationship between the distribution function of ocean nadir radiance and inherent optical properties for oceanic waters. *Applied Optics*, *48*(17), 3129–3138. https://doi.org/10.1364/AO.48.003129

Hlaing, S., Gilerson, A., Harmel, T., Tonizzo, A., Weidemann, A., Arnone, R., & Ahmed, S. (2012). Assessment of a bidirectional reflectance distribution correction of above-water and satellite water-leaving radiance in coastal waters. *Applied Optics*, *51*(2), 220–237. https://doi.org/10.1364/AO.51.000220

Hoge, F. E., Lyon, P. E., Mobley, C. D., & Sundman, L. K. (2003). Radiative transfer equation inversion: Theory and shape factor models for retrieval of oceanic inherent optical properties. *Journal of Geophysical Research*, *108*(C12), 3386. https://doi.org/10.1029/2000JC000447

IOCCG (2006). Remote sensing of inherent optical properties: Fundamentals, tests of algorithms, and applications. In Z.-P. Lee (Ed.), *Reports of the international ocean-colour coordinating group, No. 5*. Dartmouth, Canada: IOCCG.

Jerlov, N. G. (1976). *Marine optics* (230 pp.). New York, NY: Elsevier Science.

Kirk, J. T. O. (1981). Monte Carlo study of the nature of the underwater light field in, and the relationships between optical properties of, turbid yellow waters. *Marine and Freshwater Research*, *32*(4), 517–532.

Lee, M. E., & Lewis, M. R. (2003). A new method for the measurement of the optical volume scattering function in the upper ocean. *Journal of Atmospheric and Oceanic Technology*, *20*(4), 563–571. https://doi.org/10.1175/1520-0426(2003)20<563:ANMFTM>2.0.CO;2

Lee, Z., Carder, K. L., & Arnone, R. A. (2002). Deriving inherent optical properties from water color: A multiband quasi-analytical algorithm for optically deep waters. *Applied Optics*, *41*(27), 5755–5772. https://doi.org/10.1364/AO.41.005755

Lee, Z., Carder, K. L., & Du, K. (2004). Effects of molecular and particle scatterings on the model parameter for remote-sensing reflectance. *Applied Optics*, *43*(25), 4957–4964. https://doi.org/10.1364/AO.43.004957

Lee, Z., Darecki, M., Carder, K. L., Davis, C. O., Stramski, D., & Rhea, W. J. (2005). Diffuse attenuation coefficient of downwelling irradiance: An evaluation of remote sensing methods. *Journal of Geophysical Research*, *110*, C02017. https://doi.org/10.1029/2004JC002573

Lee, Z., Du, K., Voss, K. J., Zibordi, G., Lubac, B., Arnone, R., & Weidemann, A. (2011). An inherent-optical-property-centered approach to correct the angular effects in water-leaving radiance. *Applied Optics*, *50*(19), 3155–3167. https://doi.org/10.1364/AO.50.003155

Loisel, H., & Morel, A. (2001). Non-isotropy of the upward radiance field in typical coastal (Case 2) waters. *International Journal of Remote Sensing*, *22*(2–3), 275–295. https://doi.org/10.1080/014311601449934

Maffione, R. A., & Dana, D. R. (1997). Instruments and methods for measuring the backward-scattering coefficient of ocean waters. *Applied Optics*, *36*(24), 6057–6067. https://doi.org/10.1364/AO.36.006057

Mobley, C. D. (1994). *Light and water: Radiative transfer in natural waters*. San Diego, CA: Academic Press.

Mobley, C. D. (1995). *Hydrolight 3.0 users' guide*. Menlo Park, CA: SRI International.

Mobley, C. D., Gentili, B., Gordon, H. R., Jin, Z., Kattawar, G. W., Morel, A., . . . Stavn, R. H. (1993). Comparison of numerical models for computing underwater light fields. *Applied Optics*, *32*(36), 7484–7504. https://doi.org/10.1364/AO.32.007484

Mobley, C. D., Sundman, L. K., & Boss, E. (2002). Phase function effects on oceanic light fields. *Applied Optics*, *41*(6), 1035–1050. https://doi.org/10.1364/AO.41.001035

Morel, A. (1974). Optical properties of pure water and pure sea water. In N. G. Jerlov & E. S. Nielsen (Eds.), *Optical aspects of oceanography* (pp. 1–24). New York, NY: Academic Press.

Morel, A., Antoine, D., & Gentili, B. (2002). Bidirectional reflectance of oceanic waters: Accounting for Raman emission and varying particle scattering phase function. *Applied Optics*, *41*(30), 6289–6306. https://doi.org/10.1364/AO.41.006289

Morel, A., & Gentili, B. (1991). Diffuse reflectance of oceanic waters: Its dependence on Sun angle as influenced by the molecular scattering contribution. *Applied Optics*, *30*(30), 4427–4438. https://doi.org/10.1364/AO.30.004427

Morel, A., & Gentili, B. (1993). Diffuse reflectance of oceanic waters. II. Bidirectional aspects. *Applied Optics*, *32*(33), 6864–6879. https://doi.org/10.1364/AO.32.006864

Morel, A., & Gentili, B. (1996). Diffuse reflectance of oceanic waters. III. Implication of bidirectionality for the remote-sensing problem. *Applied Optics*, *35*(24), 4850–4862. https://doi.org/10.1364/AO.35.004850

Morel, A., & Mueller, J. L. (2002). Normalized water-leaving radiance and remote sensing reflectance: Bidirectional reflectance and other factors. In J. L. Mueller & G. S. Fargion (Eds.), *Ocean optics protocols for satellite ocean color sensor validation, Rev. 3, NASA/TM* (pp. 183–210). Greenbelt, MD: Goddard Space Flight Center.

Morel, A., & Prieur, L. (1977). Analysis of variations in ocean color. *Limnology and Oceanography*, *22*(4), 709–722. https://doi.org/10.4319/lo.1977.22.4.0709

Morel, A., Voss, K. J., & Gentili, B. (1995). Bidirectional reflectance of oceanic waters: A comparison of modeled and measured upward radiance fields. *Journal of Geophysical Research*, *100*(C7), 13143–13150. https://doi.org/10.1029/95JC00531

Nahorniak, J. S., Abbott, M. R., Letelier, R. M., & Scott Pegau, W. (2001). Analysis of a method to estimate chlorophyll-a concentration from irradiance measurements at varying depths. *Journal of Atmospheric Oceanic Technology*, *18*(12), 2063–2073. https://doi.org/10.1175/1520-0426(2001)018<2063:AOAMTE>2.0.CO;2

Oishi, T. (1990). Significant relationship between the backward scattering coefficient of sea water and the scatterance at 120°. *Applied Optics*, *29*(31), 4658–4665. https://doi.org/10.1364/AO.29.004658

Park, Y.-J., & Ruddick, K. (2005). Model of remote-sensing reflectance including bidirectional effects for case 1 and case 2 waters. *Applied Optics*, *44*(7), 1236–1249. https://doi.org/10.1364/AO.44.001236

Pope, R. M., & Fry, E. S. (1997). Absorption spectrum (380–700 nm) of pure water. II. Integrating cavity measurements. *Applied Optics*, *36*(33), 8710–8723. https://doi.org/10.1364/AO.36.008710

Ruddick, K., Neukermans, G., Vanhellemont, Q., & Jolivet, D. (2014). Challenges and opportunities for geostationary ocean colour remote sensing of regional seas: A review of recent results. *Remote Sensing of Environment*, *146*, 63–76. https://doi.org/10.1016/j.rse.2013.07.039

Sullivan, J. M., & Twardowski, M. S. (2009). Angular shape of the oceanic particulate volume scattering function in the backward direction. *Applied Optics*, *48*(35), 6811–6819. https://doi.org/10.1364/AO.48.006811

Weidemann, A. D., Stavn, R. H., Zaneveld, J. R. V., & Wilcox, M. R. (1995). Error in predicting hydrosol backscattering from remotely sensed reflectance. *Journal Geophysical Research*, *100*(C7), 13163–13177. https://doi.org/10.1029/95JC00459

Werdell, P. J., & Bailey, S. W. (2002). The SeaWiFS Bio-optical Archive and Storage System (SeaBASS): Current architecture and implementation. In G. S. Fargion & C. R. McClain (Eds.), *NASA Technical Memorandum TM-2002–211617*. Greenbelt, MD: NASA Goddard Space Flight Center.

Werdell, P. J., & Bailey, S. W. (2005). An improved in-situ bio-optical data set for ocean color algorithm development and satellite data product validation. *Remote Sensing Environment*, *98*(1), 122–140. https://doi.org/10.1016/j.rse.2005.07.001

Werdell, P. J., Bailey, S., Fargion, G., Pietras, C., Knobelspiesse, K., Feldman, G., & McClain, C. (2003). Unique data repository facilitates ocean color satellite validation. *Eos, Transactions American Geophysical Union*, *84*(38), 377–387. https://doi.org/10.1029/2003EO380001

Werdell, P. J., Franz, B. A., Bailey, S. W., Feldman, G. C., Boss, E., Brando, V. E., . . . Mangin, A. (2013). Generalized ocean color inversion model for retrieving marine inherent optical properties. *Applied Optics*, *52*(10), 2019–2037. https://doi.org/10.1364/AO.52.002019

Xiong, Y., Zhang, X., He, S., & Gray, D. J. (2017). Re-examining the effect of particle phase functions on the remote-sensing reflectance. *Applied Optics*, *56*(24), 6881–6888. https://doi.org/10.1364/AO.56.006881

Zaneveld, J. R. V. (1982). Remotely sensed reflectance and its dependence on vertical structure: A theoretical derivation. *Applied Optics*, *21*(22), 4146–4150. https://doi.org/10.1364/AO.21.004146

Zaneveld, J. R. V. (1995). A theoretical derivation of the dependence of the remotely sensed reflectance of the ocean on the inherent optical properties. *Journal of Geophysical Research*, *100*(C7), 13135–13142. https://doi.org/10.1029/95JC00453

Zhai, P.-W., Hu, Y., Trepte, C. R., Winker, D. M., Lucker, P. L., Lee, Z., & Josset, D. B. (2015). Uncertainty in the bidirectional reflectance model for oceanic waters. *Applied Optics*, *54*(13), 4061–4069. https://doi.org/10.1364/AO.54.004061

Zhang, X., Boss, E., & Gray, D. J. (2014a). Significance of scattering by oceanic particles at angles around 120 degree. *Optics Express*, *22*(25), 31329–31336. https://doi.org/10.1364/OE.22.031329

Zhang, X., Fournier, G. R., & Gray, D. J. (2017). Interpretation of scattering by oceanic particles around 120 degrees and its implication in ocean color studies. *Optics Express*, *25*(4), A191–A199. https://doi.org/10.1364/OE.25.00A191

Zhang, X., & Gray, D. J. (2015). Backscattering by very small particles in coastal waters. *Journal of Geophysical Research: Oceans*, *120*, 6914–6926. https://doi.org/10.1002/2015JC010936

Zhang, X., Gray, D. J., Huot, Y., You, Y., & Bi, L. (2012). Comparison of optically derived particle size distributions: Scattering over the full angular range versus diffraction at near forward angles. *Applied Optics*, *51*(21), 5085–5099. https://doi.org/10.1364/AO.51.005085

Zhang, X., Hu, L., & He, M.-X. (2009). Scattering by pure seawater: Effect of salinity. *Optics Express*, *17*(7), 5698–5710. https://doi.org/10.1364/OE.17.005698

Zhang, X., Huot, Y., Gray, D. J., Weidemann, A., & Rhea, W. J. (2013). Biogeochemical origins of particles obtained from the inversion of the volume scattering function and spectral absorption in coastal waters. *Biogeosciences*, *10*(9), 6029–6043. https://doi.org/10.5194/bg-10-6029-2013

Zhang, X., Lewis, M., Lee, M., Johnson, B., & Korotaev, G. (2002). The volume scattering function of natural bubble populations. *Limnology and Oceanogrphy*, *47*(5), 1273–1282. https://doi.org/10.4319/lo.2002.47.5.1273

Zhang, X., Stavn, R. H., Falster, A. U., Gray, D., & Gould, R. W. Jr. (2014b). New insight into particulate mineral and organic matter in coastal ocean waters through optical inversion. *Estuarine, Coastal and Shelf Science*, *149*, 1–12. https://doi.org/10.1016/j.ecss.2014.06.003